




Interseismic Coupling in the Central Nepalese Himalaya: Spatial Correlation with the 2015 Mw 7.9 Gorkha Earthquake

SHUIPING LI,¹  QI WANG,¹ GANG CHEN,² PING HE,¹ KAIHUA DING,³ YUNGUO CHEN,¹ and RONG ZOU¹

Abstract—Geodetic measurements conducted in the Himalaya over the last two decades have shown that the shallow portion of the main Himalayan thrust (MHT) was entirely locked during the interseismic period. The induced elastic strain accumulated on the MHT beneath the Lesser Himalaya was not released until the 2015 Gorkha Mw 7.9 earthquake, which ruptured the north edge of the locked portion of the MHT. We utilized our own Global Positioning System (GPS) data from southern Tibet, combined with published geodetic velocities, to quantify the spatial variations of the coupling that prevailed before the Gorkha earthquake. The refined coupling model shows that the MHT was strongly locked (coupling > 0.5) in the uppermost 15 km of crust, corresponding to a downdip width of ~ 100 km. This model suggests a sharp transition zone of strain accumulation, with a rapid decrease in the coupling coefficient from 1.0 to less than 0.2 along ~ 50 km of the MHT, coinciding with the locations of microseismicity. We also determined slip models for the 2015 Gorkha earthquake and its Mw 7.3 aftershock, considering the ramp–flat–ramp–flat structure of the MHT. We found that ~ 85% of the total moment released by the Gorkha earthquake was concentrated on the partially coupled transition portion of the MHT, indicating that the earthquake mainly ruptured the brittle/ductile transition zone. The coseismic Coulomb failure stress increased along the southern and western parts adjacent to the rupture zone, pushing these two regions closer to failure. The moment deficits that have accumulated in these regions could trigger Mw 8.0 and Mw 8.3 earthquakes, respectively.

Key words: GPS, convergence rate, interseismic coupling, 2015 Gorkha earthquake, brittle/ductile transition zone.

1. Introduction

The Himalayan orogenic belt is the most active intracontinental deformation region in the world, resulting from the continuing collision between the Indian and Eurasian plates since 50 Ma (Molnar and Tapponnier 1975). The Himalaya defines the southern margin of the Tibetan Plateau. To the south, the topography rises abruptly from an elevation of less than 1000 m in the foreland basin to more than 6000 m over a 200 km distance towards the plateau (Avouac 2003). The formation of the mountains is believed to be associated with the activation of three main thrust faults, namely the main central thrust (MCT), main boundary thrust (mbt), and main frontal thrust (MFT), which absorb a significant fraction of the shortening deformation in the Himalaya (Cattin and Avouac 2000; Lavé and Avouac 2000, 2001). Previous studies suggested that the three thrust faults imbricate within the upper crust and sole into the same mid-crust décollement, the main Himalayan thrust (MHT), which dips gently to the north beneath the Higher Himalaya and southern Tibet, with depth of 30–40 km (Fig. 1) (Nábělek et al. 2009). Global positioning system (GPS) measurements show that the present-day crustal deformation across the Himalaya is characterized by a significant shortening rate of 20 mm/year, representing nearly one half of the total convergence rate between the Indian and Eurasian plates (Bilham et al. 1997; Wang et al. 2001). The majority of the shortening across the range has been accommodated by the slip along the MHT, resulting in force to trigger large earthquakes. The shallow portion of the MHT, south of the Higher Himalaya, has been demonstrated to be frictionally locked in terms of geodetic measurements and

Electronic supplementary material The online version of this article (<https://doi.org/10.1007/s00024-019-02121-7>) contains supplementary material, which is available to authorized users.

¹ Hubei Subsurface Multi-scale Imaging Key Laboratory, Institute of Geophysics and Geomatics, China University of Geosciences, Wuhan 430074, China. E-mail: cug_lsp@foxmail.com

² College of Marine Science and Technology, China University of Geosciences, Wuhan 430074, China. E-mail: ddwhcg@cug.edu.cn

³ Faculty of Information Engineering, China University of Geosciences, Wuhan 430074, China.

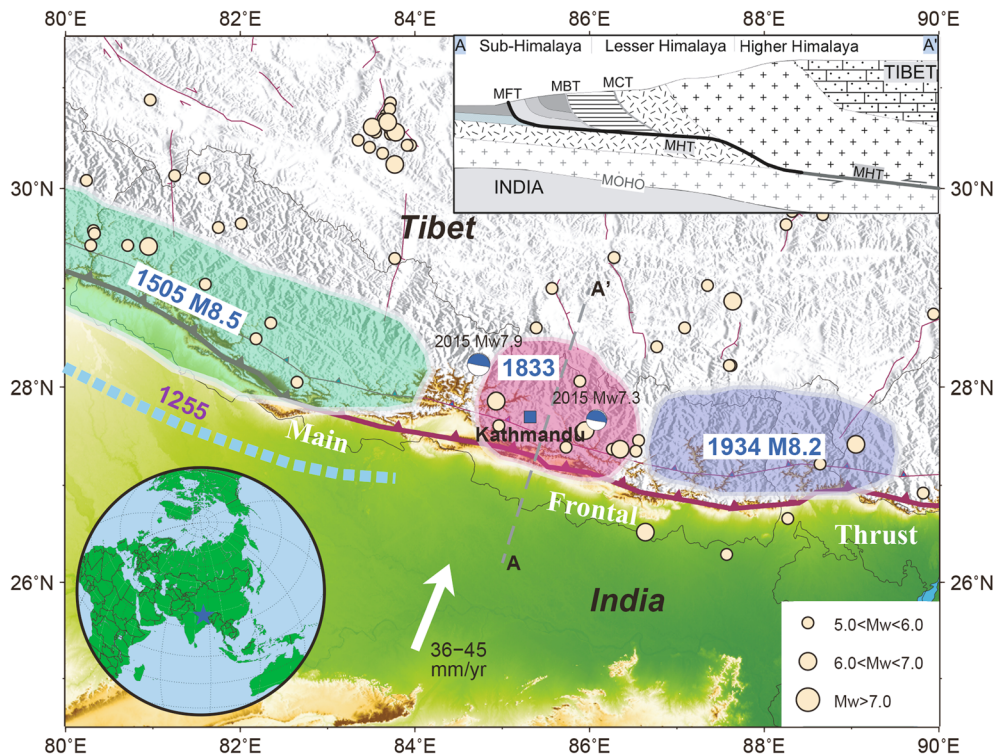


Figure 1

Seismotectonic setting and large historic earthquakes in central Nepalese Himalaya. The epicenters of the 2015 Gorkha Mw 7.9 earthquake and its Mw 7.3 aftershock are marked by two beach balls. From west to east, three earthquakes occurred sequentially in 1505 (green zone), 1833 (red zone), and 1934 (blue zone), respectively (Ambraseys and Douglas, 2004; Kumar et al. 2010; Sapkota et al. 2013). The blue dashed line indicate lateral extension of surface rupture of the 1255 earthquake. The light yellow circles indicate historical earthquakes with $M_w > 5.0$ in 1976–2016 from the CMT catalog. The location of Kathmandu is marked by a blue square. The thick white arrow shows Indian plate motion relative to Eurasia. The upper-right inset shows the topographical cross-section of transect A–A' modified from Lavé and Avouac (2001)

microseismic activities (Jouanne et al. 2004; Bettinelli et al. 2006), resulting in significant strain accumulation during the interseismic period. A portion of this strain is ultimately released during many large megathrust earthquakes, such as the 1505 $M \sim 8.5$ earthquake and the 1934 $M \sim 8.2$ earthquake in the central Himalaya (Fig. 1). More than eight $M_w > 7.5$ earthquakes have been recorded in the Himalaya over the past 500 years (Bilham and Ambraseys 2005). Although the coseismic ruptures of these larger events, in responding to interseismic strain accumulation, have partially released the elastic energy, a moment deficit remains to be balanced in the future, which could contribute to devastating earthquakes (Stevens and Avouac 2016; Xiong et al. 2017).

Interseismic coupling plays an important role in assessing earthquake potential and recurrence, and is commonly employed to model the strain accumulation state (Bollinger et al. 2004; Avouac et al. 2015). GPS measurements in several subduction zones, such as those of Chile, Sumatra, the Andes, and Japan, have exhibited heterogeneous coupling patterns on plate boundary faults, suggesting that the plate interface in the 0–40 km seismogenic depth range consists of interfingered patches that either remain locked or creep aseismically (Suwa et al. 2006; Prawirodirdjo et al. 2010; Chlieh et al. 2011). In the Himalaya, the coupling pattern on the MHT has been constrained by geodetic measurements. Ader et al. (2012) proposed a coupling model in the Nepal Himalaya, showing that the MHT is locked from the

surface to a downdip width of ~ 100 km. Stevens and Avouac (2015) estimated the strain accumulation along the whole Himalayan arc, suggesting that coupling on the MHT behaves homogeneously with a seismic moment accumulation rate of $15.1 \pm 1 \times 10^{19}$ Nm/year. These studies have described the first-order characteristics of the strain budget on the MHT. However, most previously established GPS stations are situated in the foothills of the Himalaya. GPS sites in southern Tibet are sparse. The coupling variation beneath the Higher Himalaya remains ambiguous. In addition, most previous studies have suggested that seismic slips during large earthquakes tend to occur in areas that remain locked during the interseismic period (Chlieh et al. 2011; Métois et al. 2012). Nonetheless, the correlation between coseismic slips and interseismic coupling in the Himalaya is still poorly understood, owing to the lack of large earthquakes documented in terms of seismic waveforms or geodetic observations.

The 2015 Mw 7.9 Gorkha earthquake occurred in central Nepal along the higher Himalaya. The hypocenter depth was 15 km, indicating that this event appears to have occurred at the interface of the MHT (Bai et al. 2016; McNamara et al. 2017; Arora et al. 2017). The Gorkha event is the first occurrence of a large continental thrust earthquake in Himalaya to be concurrently recorded in terms of geodetic and seismic measurements, providing a rare opportunity to explore the correlation between the interseismic coupling and coseismic rupture. It is well known that a large earthquake is likely to rupture the most strongly coupled segments. Analyzing the spatial correlation between the interseismic coupling and coseismic slip distribution is helpful for understanding the balance of the seismic moment accumulation and release (Morsut et al. 2017). In this study, we utilized GPS data surveyed in southern Tibet together with published geodetic velocities to derive a complete velocity field in the central Nepalese Himalaya. This new velocity field is then employed to refine the convergence rates across the central Nepalese Himalaya. Considering the ramp–flat–ramp–flat geometry of the MHT, we calculated the interseismic coupling using triangular dislocation. We also determined the coseismic slip distribution of the Gorkha earthquake to analyze the spatial correlation

between the interseismic coupling and coseismic rupture features.

2. GPS Data and Analysis

2.1. GPS Data Processing

The GPS velocities recorded in the central Nepalese Himalaya mainly consist of results from the Crustal Movement Observation Network of China (CMONOC) project (Wang et al. 2017) and published studies (Bettinelli et al. 2006; Bilham et al. 1997). In addition, we began recording GPS measurements in southern Tibet in 1999, and have obtained GPS data for approximately 40 sites with an occupation of more than 36 h for each survey. At least three periods of observation were conducted for each site. All the data were recorded prior to the occurrence of the 2015 Gorkha earthquake. The CMONOC data and our own data were processed using the GIPSY-OASIS-II software (Zumberge et al. 1997). The data analysis followed the procedures adopted by Fu and Freymueller (2012). We utilized the Jet Propulsion Laboratory's (JPL's) reanalyzed IGS08 orbit and clock products, and refined the absolute antenna phase center models for both the GPS receiver and satellite antennas. We utilized the global mapping function (GMF) tropospheric mapping function and the global pressure and temperature (GPT) model to reduce the tropospheric delay error, and the ocean tide model TPXO7.0 to correct for ocean tide loading. Finally, we obtained a set of GPS velocity fields under a unified reference frame by completing a seven-parameter Helmert transformation through some common sites that occur within the different datasets. The differences in the EW and NS components of the common stations between different datasets are generally smaller than 1.2 and 1.0 mm/year, respectively. Figure 2a shows the combined velocity field for ~ 120 sites in the central Nepalese Himalaya relative to the stable Eurasian reference frame. The mean uncertainty of GPS velocities is ~ 1.5 mm/year.

It should be noted that the majority of GPS velocities in southern Tibet are derived from campaign-model measurements. The use of vertical

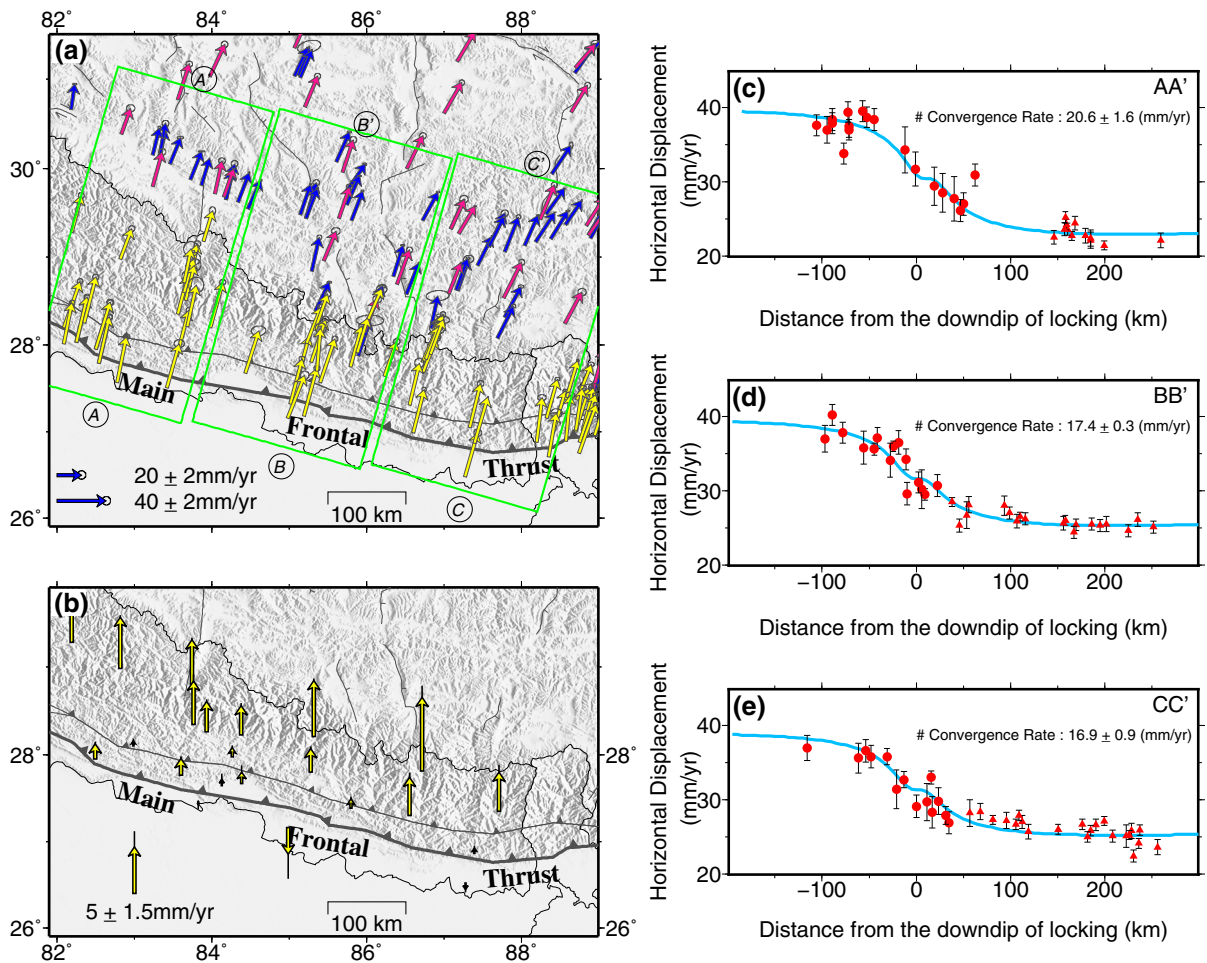


Figure 2

GPS velocity field in the central Nepalese Himalaya. **a** Horizontal GPS velocities relative to the Eurasia reference frame (with 95% confidence ellipses). The yellow arrows represent GPS velocities from published studies (Ader et al. 2012; Bettinelli et al. 2006). The red arrows show the velocities of the campaign and continuous sites from the CMONOC project. Our own ~ 40 GPS velocities in southern Tibet are plotted as blue arrows. The three green boxes indicate the locations of the velocity profiles (AA', BB', CC') perpendicular to the Himalayan arc. **b** GPS vertical velocities in Nepal relative to the India reference frame. **c–e** GPS horizontal velocity profiles and calculated convergence rates. The red circles and triangles with error bars represent the velocity components parallel to the azimuth of each profile with uncertainties of one standard deviation. The triangles denote the velocity components of our own data and the CMONOC data. The blue solid lines indicate the model predictions

velocities in southern Tibet remains challenging, owing to the limited observation timespan. Commonly, the vertical positioning precision of GPS measurements is typically 2–2.5 times lower than that of the horizontal. Furthermore, in southern Tibet the magnitude of the crustal vertical velocity is usually considerably smaller than that of the horizontal velocity (Liang et al. 2013). Therefore, the vertical velocities in southern Tibet are not adopted in the

modeling. In central Nepal, a network of continuous GPS (cGPS) stations have been installed since 1997 by Caltech in order to monitor and determine present-day velocities in the Himalaya (Ader et al. 2012). Such a long time span of observations makes it possible to acquire reliable vertical deformations in this region. Data from the time of installation of the cGPS stations to the day before the Gorkha earthquake were analyzed by Jouanne et al. (2017) using

the Bernese software. These vertical velocities (relative to the India reference frame, as shown in Fig. 2b) enhance the spatial density of observations for the coupling model. These are utilized in the coupling inversion approach presented below, although we find that they do not add much constraint to the model.

2.2. Estimation of Convergence Rate

An important goal in Himalayan studies during recent decades has been to refine the Himalayan convergence rate, as this is responsible for the productivity of Himalayan earthquakes. In coupling inversion, the long-term convergence rate across the Himalaya is also an important reference value, as described in Sect. 3. Here, we incorporate the new GPS data from southern Tibet to further constrain the Himalayan convergence rate. Following most previous investigations (e.g., Bilham et al. 1997; Bettinelli et al. 2006), we modeled the interseismic strain resulting from slips along a creeping dislocation embedded in an elastic half-space. These dislocations represent the aseismic shear north of the locked portion of the Himalayan detachment system. Three velocity profiles were projected along the azimuth of convergence (N16°E). The length and width for each profile were ~ 200 km and ~ 110 km, respectively. We assumed that the thrusting slip on a detachment fault dominated in every profile across the Himalayan orogenic belt, ignoring lateral variations in the thrust slip in accordance with the two-dimensional (2D) edge dislocation model. The analytical solution for a pure dip slip fault can be written as follows (Freund and Barnett 1976):

$$v = \frac{s}{\pi} \left[\frac{h^2 \cos \alpha + xh \sin \alpha}{h^2 + x^2} + \sin \alpha \tan^{-1}(x/h) \right] \quad (1)$$

where v represents the site velocity normal to the Himalayan arc, s denotes the thrusting rate on a major detachment fault, and h and α are the locking depth and fault dip, respectively. Furthermore, x indicates the horizontal distance to the trace of the fault.

Moderate-sized earthquakes ($5 < M_s < 6$) and smaller magnitude events ($m_L < 4$) in the central Himalaya are confined to 10–20 km in depth (Molnar and Chen 1984; Pandey et al. 1995). The INDEPTH

seismic reflection profile in eastern Nepal exhibits a discrete fault plane dip of $\sim 9^\circ$ (Zhao et al. 1993). Supposing that the aforementioned fault geometry can be applied elsewhere in the central Nepalese Himalaya, the locking depth of the MHT can be fixed at 20 km with a dip of $\sim 9^\circ$. The weighted least-squares method was adopted to estimate the convergence rate.

The 2D dislocation model provided an adequate fit to the observed GPS velocities (Fig. 2c–e). The root-mean-square (RMS) errors of the post-fit residuals for each velocity profile were always less than 3 mm/year, which is broadly compatible with the formal uncertainties of observed velocities, suggesting that few if any unmodeled biases remained. The inverted slip rates were not strongly affected (a change of less than 2 mm/year) by the parameters of the locking depth and fault dip in the range of $15 \text{ km} < \text{locking depth} < 25 \text{ km}$ and $4^\circ < \text{fault dip} < 12^\circ$, indicating that the trade-off effect between the convergence rate and fault geometry was moderate.

In west-central Nepal (profile AA'), the estimated convergence rate is 20.6 ± 1.6 mm/year, which is comparable to the 20.2 ± 1.1 mm/year estimated by Stevens and Avouac (2015). In the central Nepalese Himalaya (profile BB'), GPS observations yield a convergence rate of 17.4 ± 0.3 mm/year, which is slightly lower than the 21.5 ± 2.5 mm/year determined by the Holocene river terraces (Lavé and Avouac 2000). This result implies that a small fraction of the active convergence of the Himalayan orogen might not be accommodated by slips along the MHT. In the eastern Nepalese Himalaya (profile CC'), GPS measurements suggest a convergence rate of 16.9 ± 0.9 mm/year, which is consistent with the slip rate of 16 mm/year determined by Banerjee et al. (2008). In general, the convergence rate decreases from the west-central to the eastern Nepalese Himalaya. The along-strike variations for convergence rates could reflect the postseismic viscoelastic relaxation effects caused by large earthquakes, because many GPS sites lie within or adjacent to the epicentral areas of large Himalayan earthquakes, and the GPS velocities are inevitably more or less biased by the residual postseismic deformations from large megathrust earthquakes. The postseismic

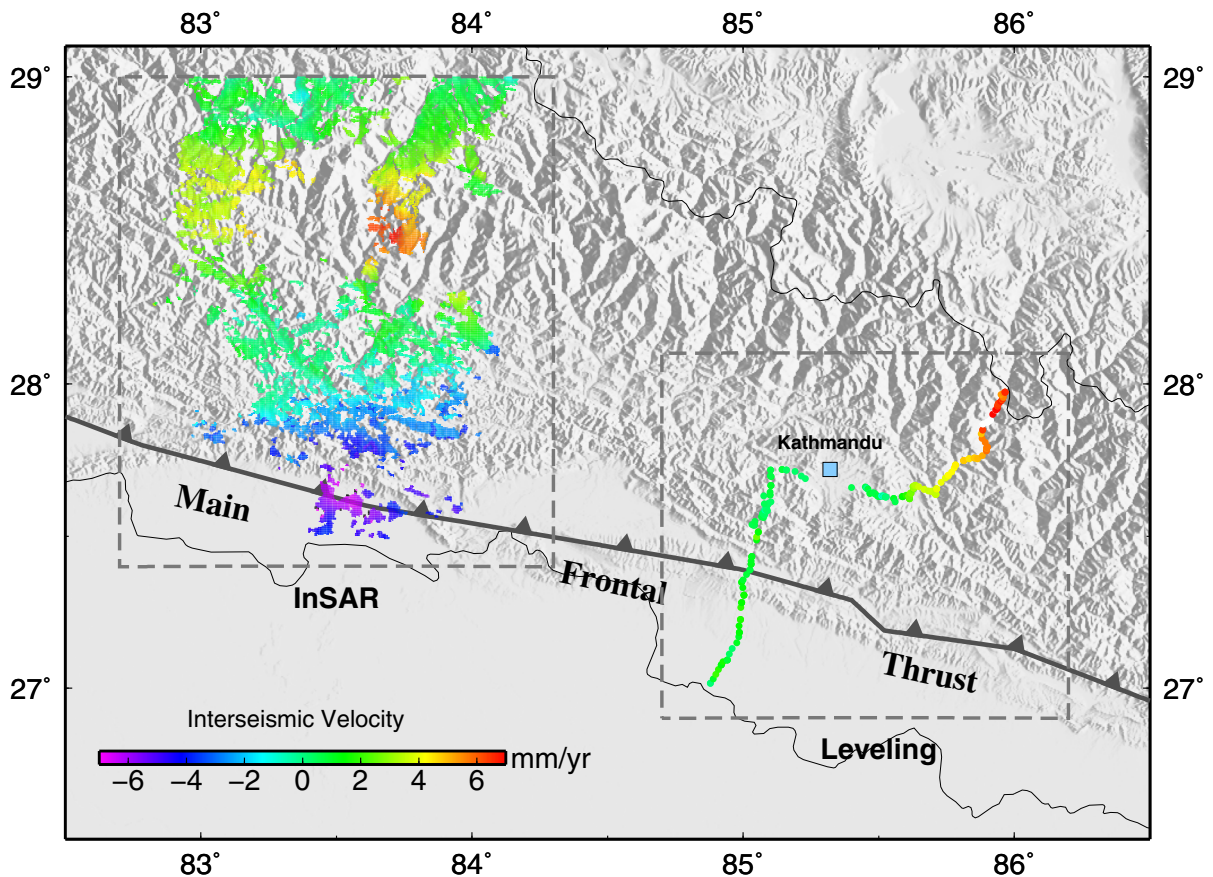


Figure 3
Observed interseismic InSAR and leveling velocities in central Nepalese Himalaya

effects caused by the 1934 Bihar–Nepal $M \sim 8.2$ earthquake on the interseismic convergence rates are evaluated and discussed in Sect. 5.1. It is worth noting that because of our broader and denser distribution of GPS data in southern Tibet, the estimated convergence rates can provide more tightly constrained upper bounds.

3. Modeling the Interseismic Coupling in Central Nepal

The resolved coupling image can benefit from a refined spatial density of observations, including vertical deformation rates. In addition to the GPS vertical velocities in Nepal, we also collected all the available interseismic interferometric synthetic aperture radar (InSAR) and leveling data in the central

Himalaya in order to determine the coupling parameters, although they are only localized in two narrow profiles (Fig. 3) (Grandin et al. 2012; Jackson and Bilham 1994). Owing to the highly rugged and heavy vegetation terrains in the Himalaya, as of now only one stripe of SAR C-band images acquired by the ENVISAT satellite on track 119 (descending) between 2003 and 2010 has successfully been processed. For satellite SAR images, the small baseline subsets (SBAS) processing strategy was exploited to produce interferograms. In addition, a slope-adaptive spectral shift range filtering method was applied during interferogram formation to reduce the geometric decorrelation resulting from steep terrain slopes in central Nepal. After interferogram unwrapping and geocoding, the line-of-sight (LOS) displacement velocity maps and corresponding time-series were retrieved (Readers interested in the

information of ENVISAT SAR processed with the SBAS method may refer to the work of Grandin et al. (2012)). The InSAR profile shows a gentle increase of the uplift rate toward the North, with a peak uplift rate of 7 mm/year (~ 100 km north of the MFT). To reduce the burden of calculation in inversion, a quad-tree algorithm was employed to down-sample the velocities (He et al. 2016). For the leveling data, we followed previous studies to remove the points in the Kathmandu Valley that are undergoing obvious subsidence (Grandin et al. 2012). Finally, 63 InSAR and 152 leveling velocities are included in the coupling inversion.

We adopted the back-slip modeling approach (Savage 1983) to solve for the slip rate deficit along the MHT. This model assumes that the hanging wall does not deform over the long term, and only applies to the case of a planar fault. However, it remains a valid approximation even if the megathrust is not strictly planar in reality (Vergne et al. 2001). In our modeling, the geometry of the MHT was characterized by four connected fault portions dipping northward from the MFT (Elliott et al. 2016): first, a shallow ramp with a dip of 30° between the surface and a 5 km depth; second, a flat detachment with a dip of 7° extending from a depth of 5 km to 15 km; third, a mid-crust ramp that has a larger dip angle of 20° at 15 to 25 km; and finally a sub-horizontal

décollement with a dip of 6° beneath the Higher Himalaya. These four fault segments constitute the “ramp–flat–ramp–flat” structure of the MHT (Fig. 4). The strike of the interface is fixed at 285° . We extended the model fault downward with a width of 400 km from the MFT to avoid edge effects. Meanwhile, such an expanded downdip width can better constrain the slip rate deficit at a large depth using our own GPS data in southern Tibet. The entire interface of the MHT is discretized into a 93×20 matrix of rectangular subfaults, each with dimensions of $20 \text{ km} \times 20 \text{ km}$. To achieve seamless gridding on the model plane, each subfault was approximated by two triangular dislocation elements (TDEs). As a result, a total of 1860 TDEs were employed, for which we calculated the Green’s function using angular dislocation in an elastic half-space (Meade 2007).

We calculated the coupling coefficient (ϕ) for each patch based on the following equation (Cheloni et al. 2014):

$$\phi = \frac{V_d}{V_c} \quad (2)$$

where V_d is the slip rate deficit on a fault patch and V_c represents the long-term block convergence rate over many earthquake cycles. The slip deficit rate is constrained to be positive and no larger than the long-

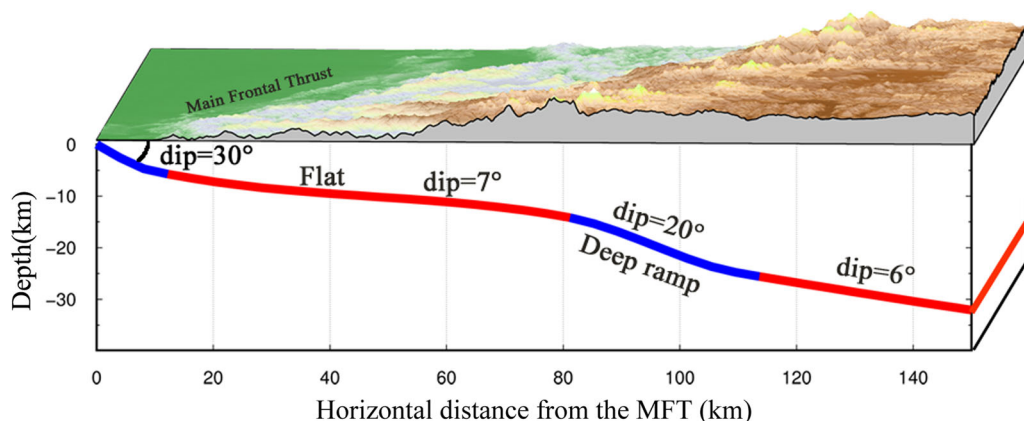


Figure 4

Cross section of the MHT interface used in the modeling. The two blue lines indicate the shallow and mid-crust ramps. The red lines denote the flat structures of the MHT

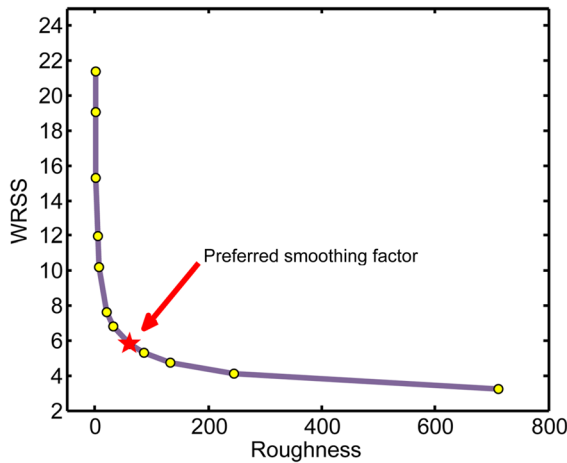


Figure 5

Trade-off curve between model roughness and WRSS during the inversion of the coupling distribution. The red pentagram represents the optimal smoothing factor

term convergence rate, so that the coupling coefficient can be constrained between 0 and 1. A coupling value of 0 means that the MHT is creeping at the long-term convergence rate, and a coupling of 1 means that there is no creep on the MHT during the interseismic period (i.e., it is fully locked). A coupling value between 0 and 1 means that the fault is partially locked.

The optimal slip rate deficits can be solved through the linear equation

$$\begin{bmatrix} d^p \\ 0 \end{bmatrix} = \begin{bmatrix} G^{e,p} \\ k^2 \nabla^2 \end{bmatrix} s^e. \quad (3)$$

The optimal objective function can be described as follows:

$$\|W(Gs - d)\|^2 + k^2 \|\nabla^2 s\|^2 = \min, \quad (4)$$

where d^p represents the displacement at point (p) on the surface caused by the slip (s^e) on the triangular elements (e) of a buried fault, $G^{e,p}$ denotes the Green's function matrix, ∇^2 represents the smoothing operator to avoid a slip anomaly between neighboring elements, k^2 is the smoothing factor based on the visual inspection of the trade-off curve between the model roughness and the weighted residual sum of squares (WRSS) (Fig. 5), and W is the weight matrix combining the GPS (including the horizontal and vertical components), InSAR, and leveling

observations. In the joint inversion, the datasets are weighted based on the trade-off curve between solution misfit and the optimum weight ratio between GPS and InSAR-leveling data (Xu et al. 2009; Yi et al. 2017). The non-negative least-squares algorithm was applied to solve the slip on each patch (Lawson and Hanson 1974). We utilized a scale-dependent umbrella operator to regularize the fault-slip distribution (Maerten 2005). The operator is defined as follows:

$$\nabla^2 s_i = \frac{2}{L_i} \sum_{j=1}^3 \frac{s_j - s_i}{h_{ij}}, \quad (5)$$

where h_{ij} denotes the distance from the center of the element i to the adjacent j th element, and L_i and s_i are the sum of the element center distances and the slip vector of the i th element, respectively.

4. Results

4.1. Coupling Characteristics

The best-fitting coupling model along the MHT, derived from joint inversion of the GPS, InSAR, and leveling data, is illustrated in Fig. 6a. We illustrate the fitness to the GPS, InSAR and leveling observations in Fig. 7. The mean misfits of the GPS horizontal and vertical components are 1.38 and 1.47 mm/year, respectively, exhibiting small velocity residuals. The mean misfits of the InSAR and leveling data are 0.7, and 0.4 mm/year, respectively. The reduction in the data variance is $\sim 91\%$ for the GPS horizontal measurements, $\sim 82\%$ for GPS vertical velocities, $\sim 86\%$ for the leveling data, and $\sim 92\%$ for the InSAR observations, suggesting that the geodetic observations can be satisfactorily explained by the model.

In general, the MHT is fully locked along the strike of the Himalaya, with no obvious shallow creeping zone identified, and exhibits a homogeneous coupling pattern. Unlike the coupling characteristics along strike, the coupling distribution along the downdip direction exhibits obvious spatial variations. To illustrate the details of the coupling variation, three arc-normal profiles of the coupling coefficient were projected (Fig. 6b). These profiles show the

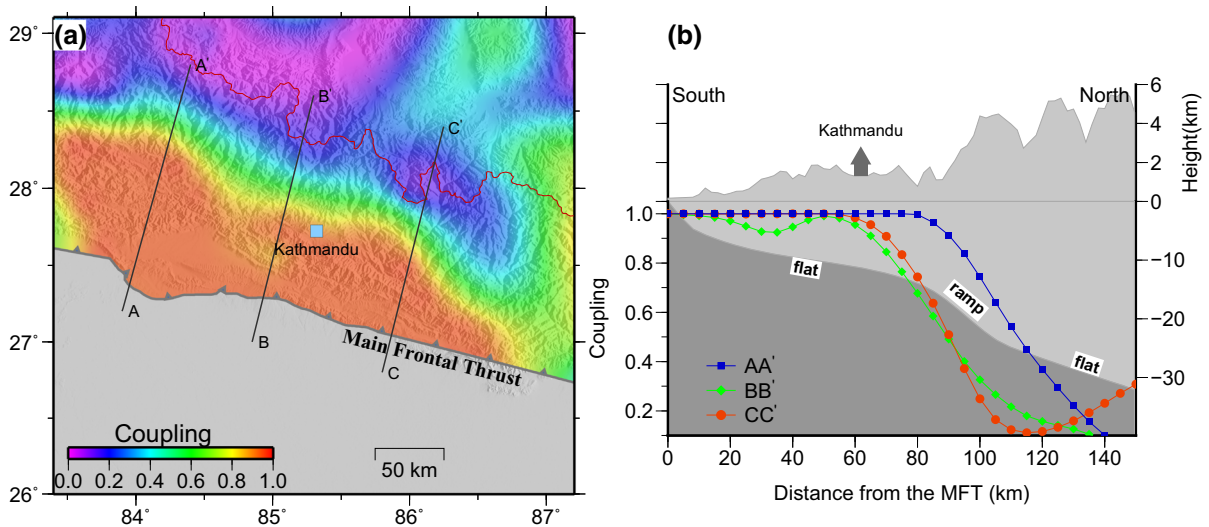


Figure 6

a Interseismic coupling model in central Nepalese Himalaya. **b** Three coupling profiles perpendicular to the mountain range

smooth distribution of the coupling coefficient with respect to the downdip width. From the coupling profiles, we can observe the following. First, the MHT under the sub-Himalaya and Lesser Himalaya is fully coupled. Nevertheless, the mid-crust ramp beneath the front of the Higher Himalaya is partly coupled, suggesting that this ramp is affected by aseismic creeping. This result is different from the 100% coupling of the mid-crust ramp found by a previous study (Ader et al. 2012). Second, maximal creeping (with coupling as low as 0.2) is observed north of the mid-crust ramp. The free creeping zones always correspond to rate-strengthening areas, which probably act as barriers resisting fault ruptures. Third, if we consider a coupling coefficient of 0.5 as the boundary value to distinguish fault locking or creeping, then the locking width west of Kathmandu (profile AA') is ~ 110 km, which is slightly longer than the locking width of ~ 90 km east of Kathmandu (profile CC'). The average locking width of ~ 100 km in the central Nepalese Himalaya is reasonably consistent with previous estimations (Ader et al. 2012; Stevens and Avouac 2015; Jouanne et al. 2017).

A sharp transition zone where the fault interface gradually decouples from full locking to free creeping ($0.2 < \phi < 1.0$) can be identified beneath the front of

the Higher Himalaya. The width of this transition zone at the longitude of Kathmandu (profile BB') is approximately 50 km, which is considerably shorter than the typical range of subduction zones (Lay et al. 2012). The sharpest transition zone corresponds to an area where the resolution is enhanced by the leveling data. This transition zone coincides spatially with the location of the mid-crust ramp (Fig. 6b), suggesting that the geometric structure of the MHT influences the coupling status at the interface. The modeled maximal uplift rates reach 6 mm/year in the high chain of the central Nepalese Himalaya, which is slightly less than the maximal observed uplift of 8 mm/year from leveling measurements (Fig. 7c). This discrepancy probably indicates that the real dip of the mid-crust ramp might be slightly greater than 20° (which was adopted in this study). In addition, the ongoing glacial isostatic adjustment induced by the current melting of the Himalayan glaciers might also contribute to the larger observed uplift rate than that of the modeling (Duputel et al. 2016).

4.2. Resolution Test

A series of checkerboard tests were performed to evaluate the spatial resolution of the coupling image. We imposed alternating slip rates of 20 mm/year (full

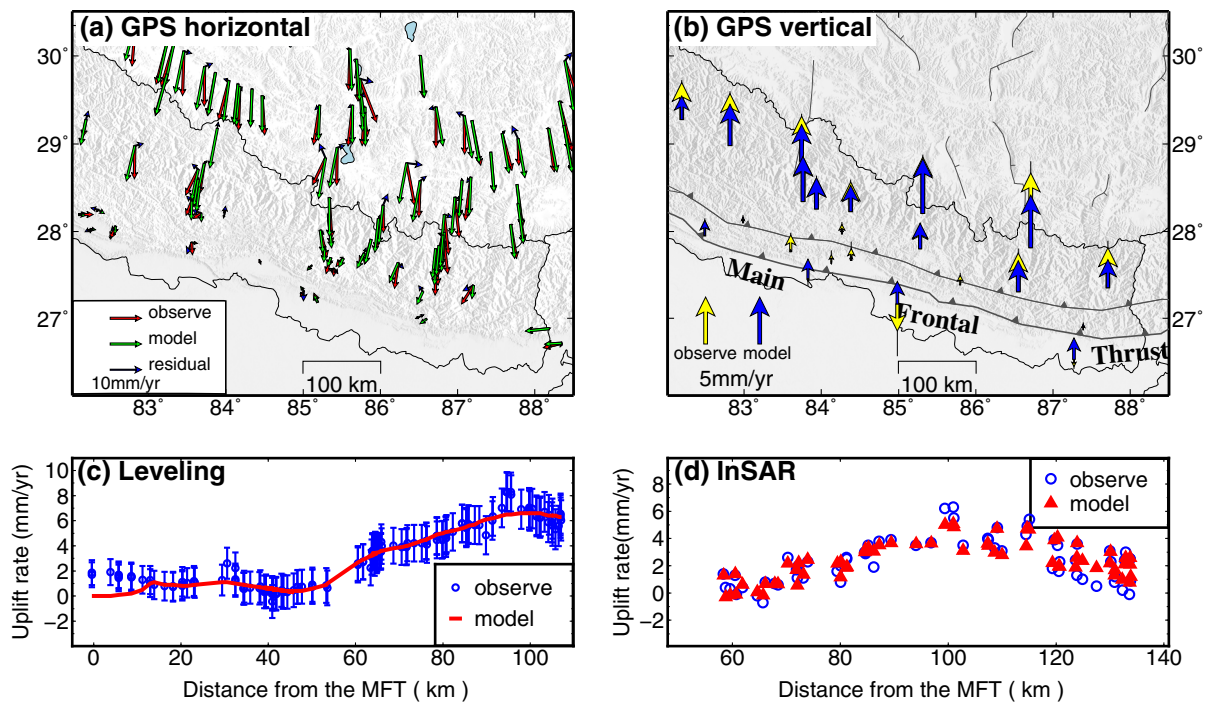


Figure 7

Post-fit residual of the GPS data and the misfit to the InSAR and leveling observations. **a** The fitness to the GPS horizontal velocities. The red, green, and blue arrows represent the observed, predicted, and residual GPS horizontal velocities, respectively. **b** The fitness to the GPS vertical velocities. The yellow and blue arrows indicate the observed and predicted velocities, respectively. **c** Leveling velocities along the profile perpendicular to the MFT. The blue circles with error bars show the observed leveling velocities, and the red solid line represents the model prediction. **d** InSAR velocities along the transect perpendicular to the MFT. The blue circles and red triangles denote the observed and simulated InSAR velocities, respectively

locking) and 0 mm/year (free creeping) on the input checkerboard patches. The surface velocities (GPS, InSAR, and leveling) were synthesized by the input model. The synthetic data were disturbed by Gaussian noise, which followed a normal distribution with zero mean and standard deviation for the observed data. We inverted the noisy velocities using the same strategy as for the real data. The results for the checkerboard tests are illustrated in Fig. 8. In general, the resolution decays as the checkerboard dimension decreases. When the patch of the checkerboard is approximately 50 km, the input coupling distribution can be retrieved effectively except for the part from the western portion to Kathmandu ($84^{\circ} - 85^{\circ}E$), on account of the sparse data in this region. A patch size of ~ 30 km along the downdip direction near Kathmandu can be resolved owing to the incorporation of leveling data, which is smaller than the width of the coupling transition zone in central Nepal (~ 50 km),

suggesting that this transition zone can be retrieved by surface geodetic measurements. In general, the main features of fault coupling can be resolved in terms of both size and pattern using geodetic data.

5. Discussion

5.1. Viscoelastic Effects on the Convergence Rate and Coupling

Previous studies have indicated that postseismic deformation induced by great earthquakes $M > 8$ in Mongolia and Chile may persist for several decades, or even a century (Vergnolle et al. 2003; Lorenzo-Martín et al. 2006). In the Himalaya, the geodetic measurements were all obtained in recent decades, with some of them located close to the epicentral area of the 1934 $M \sim 8.2$ earthquake. This large

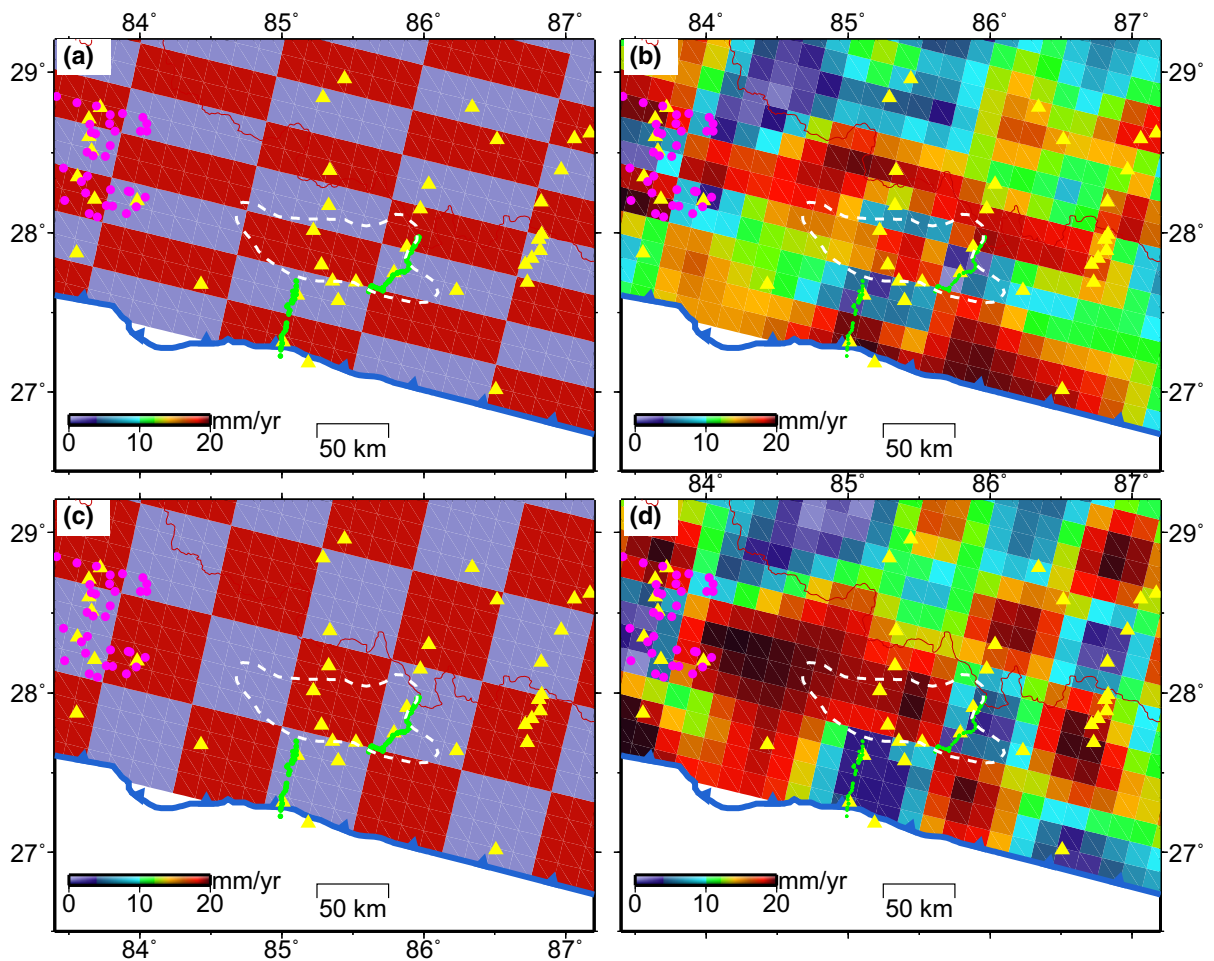


Figure 8

Checkerboard tests showing the spatial resolution of the fault coupling based on the joint inversion of the GPS, leveling, and InSAR data. **a** and **c**: Synthetic input slip distributions used to create the synthetic deformation field. **b** and **d**: Recovered slip patterns inverted from the synthetic surface deformation. The yellow triangles denote the locations of GPS sites. Green and pink points show the locations of leveling and InSAR data, respectively. The white dashed line outlines the rupture zone of the 2015 Gorkha earthquake

megathrust earthquake may still be contributing a small postseismic signal, which could affect the interseismic velocities and the estimated convergence rates. In order to test the possible magnitude of this effect, we adopt a simple source model according to the seismic moments (Chen and Molnar 1977) and a scaling law for the relation between the rupture size and seismic moment (Feldl and Bilham 2006; Sapkota et al. 2013). A 2D rheologic structure for the Himalaya and southern Tibet is considered in our viscoelastic model (Fig. 9a). We select the steady-

state viscosities for the lower crust and upper mantle from two recent studies on the postseismic deformation of the 2015 Gorkha earthquake (Zhao et al. 2017; Wang and Fialko 2018). We employ the spectral element method code VISCO2.5D to calculate the deformation resulting from viscoelastic relaxation in the lower crust and upper mantle of Tibet and India caused by the 1934 event (Pollitz 2014). The results are illustrated in Fig. 9b. For sites to the north of the earthquake source area, notable southward motions can be identified with a maximum value of 2.7 mm/

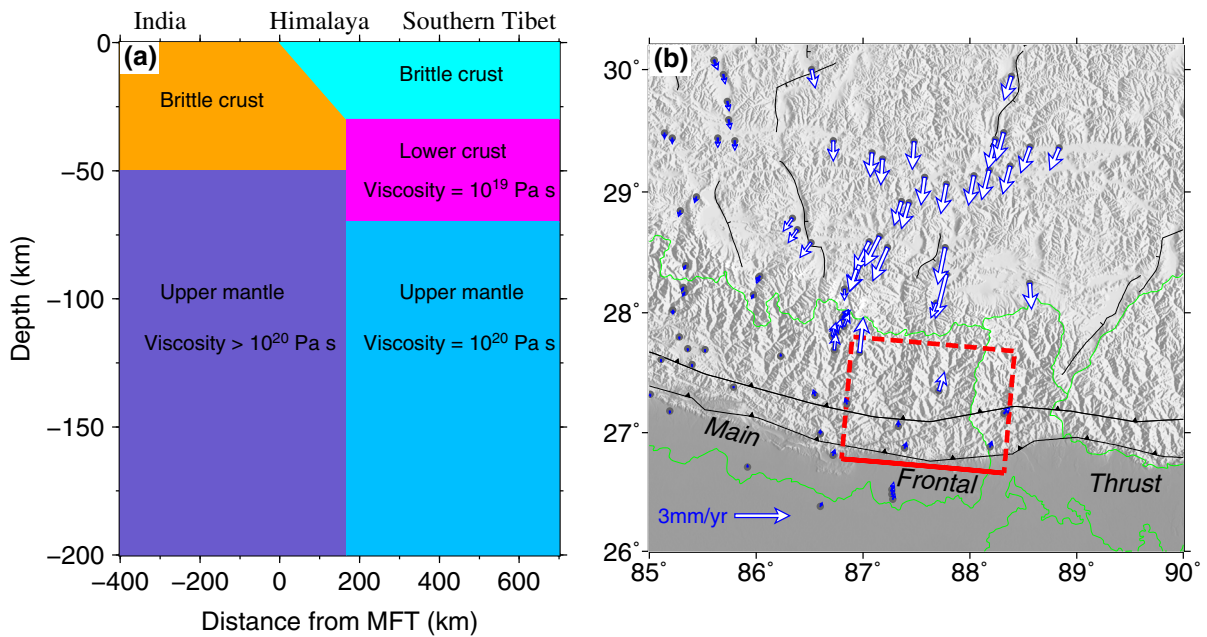


Figure 9

a Rheological model structure across the central Nepalese Himalaya. **b** Simulated postseismic deformation at the locations of GPS sites in eastern Nepal induced by the viscoelastic relaxation 80 years after the 1934 Bihar–Nepal $M \sim 8.2$ earthquake. The red square indicates the earthquake source area

year. For sites just above the source area, ongoing northward motions of 1–2 mm/year are suggested. This kind of contraction suggests that the continued relaxation caused by the 1934 earthquakes would increase the interseismic convergence rate across the eastern Nepalese Himalaya. In fact, the convergence rate across the western Nepalese Himalaya, where no large earthquakes have occurred for several centuries, is 3–4 mm/year larger than that across the eastern Nepalese Himalaya, while the opposite would be expected according to the modeling. Thus, the model prediction cannot account for the apparent differences in convergence rates between the eastern and western Nepal Himalaya. If we removed the postseismic contributions from GPS velocities, then the along-strike differences in the long-term convergence rates between the eastern and western Nepalese Himalaya might be even larger. We note that the coupling pattern in the central Nepalese Himalaya is barely modified after removing the postseismic effects caused by the 1934 earthquake, although the transition zone of the coupling is slightly broadened compared to the original coupling map.

5.2. Spatial Correlation Between Interseismic Coupling and Coseismic Slip

Only two large earthquakes ($M_w > 7.5$) have occurred along the Nepal Himalaya during the past century: the 1934 Bihar–Nepal earthquake ($M \sim 8.2$) in eastern Nepal and the 2015 Gorkha earthquake ($M_w 7.9$) in central Nepal. The detailed coseismic slip distribution for the 1934 earthquake is particularly uncertain, thus preventing a comparison with the interseismic coupling (Sapkota et al. 2013). The 2015 Gorkha earthquake nucleated ~ 80 km northwest of Kathmandu, and failed a 150 km long segment of the MHT (Avouac et al. 2015). The rupture image of the Gorkha earthquake is now well documented by seismic and geodetic observations (Galetzka et al. 2015; Grandin et al. 2015), allowing a detailed comparison with the pattern of fault locking.

Before assessing the spatial correlation between the coseismic slip distribution and interseismic coupling, we developed a geodetically constrained slip distribution of the Gorkha earthquake on the same fault geometry as used in the coupling estimation (Fig. 10a). The detailed process for the slip inversion

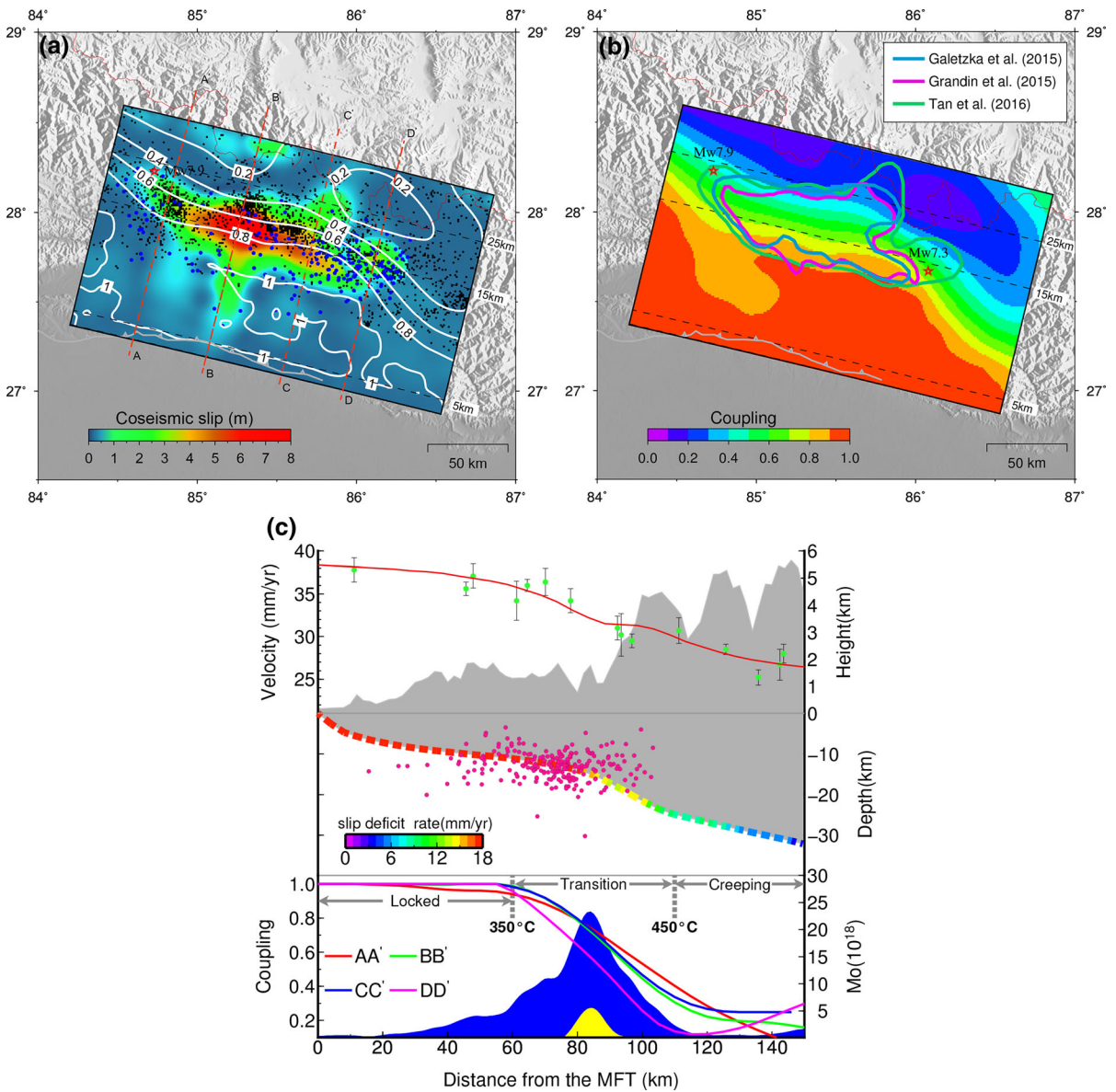


Figure 10

Map view illustrating the spatial correlation between the interseismic coupling and coseismic slip distribution of the 2015 Mw 7.9 Gorkha earthquake. **a** The colored basemap shows the coseismic fault slip. White contour lines denote the interseismic coupling distribution. Black dots show small background earthquakes derived by Pandey et al. (1995). Blue circles mark the locations of aftershocks according to Bai et al. (2016). The four red dashed lines indicate the locations of four coupling profiles (AA', BB', CC', DD'). **b** The blue-to-red basemap indicates the coupling distribution. The blue, red, and green solid lines outline the spatial extent of the rupture of the Gorkha earthquake based on three different studies (Galetzka et al. 2015; Grandin et al. 2015; Tan et al. 2016). **c** Fault profile perpendicular to the MFT. Top: The green dots with error bars represent horizontal GPS velocities, and the red line denotes the model prediction. Middle: The thick dashed line denotes the interface of the MHT and its color represents the slip deficit rate calculated by the coupling coefficient and convergence rate. Red circles indicate the relocated aftershocks. Bottom: Blue and yellow histograms indicate the distributions of the moment release of the Mw 7.9 mainshock and the Mw 7.3 aftershock. The four solid lines (red, blue, green, and pink) show the coupling profiles along the downdip direction

is reported in the auxiliary material (Text S1, Figs. S1–S5). The coseismic slip model exhibits an elongated unilateral rupture, with a maximal slip of

7.8 m. In addition, three previous rupture models derived from the inversion of geodetic and seismological data are also included for comparison with the

interseismic coupling (Fig. 10b). Comparing Figs. 10a and b, we conclude that the spatial extents of the four slip models behave consistently, although their maximal slip magnitudes exhibit slight differences.

The spatial correlation between the interseismic coupling and coseismic slip distribution suggests that the Gorkha earthquake unzipped the lower edge of the locked portion of the MHT, in accordance with the conclusion proposed by Avouac et al. (2015). As shown in Fig. 10a, the Gorkha earthquake initiated from the epicenter, where the coupling coefficient was ~ 0.5 , and then propagated laterally in the ESE direction. In general, interseismic coupling behaves homogeneously along the propagation direction of the rupture. The fault patches are estimated to have slipped ≥ 4 m, corresponding to an area of the interface in which $0.5 < \text{coupling} < 0.8$, with a peak slip near a region coupled at ≥ 0.7 . The updip end of the rupture stopped at the leading edge of the Lesser Himalaya, with a coupling coefficient of ~ 1.0 , leaving the shallow fully locked part unbroken. In the downdip direction, the coseismic slip terminated almost at the bottom of the mid-crust ramp. This result closely agrees with the decreased coupling (< 0.2) limiting the propagation of the rupture to a greater depth. This characteristic indicates that the ruptures of large megathrust earthquakes in the Himalaya can fail patches that are inferred to be less strongly coupled (as low as 0.2).

In more detail, our modeling suggests that the Gorkha earthquake appears to have mainly ruptured the transition zone of coupling on the MHT. This is demonstrated by the distributions of the moment release along the downdip direction (Fig. 10c). For the mainshock, approximately 85% of the released moment was concentrated on the partially locked transition zone, where the coupling decreases from 1.0 to less than 0.2. Only $\sim 15\%$ of the released moment was in the upper fully locked portion. For the Mw 7.3 aftershock, all the released energy was confined to the transition zone of the coupling (Fig. 10c). In the map view, this brittle/ductile transition zone is followed by a narrow belt of background seismicity (Fig. 10a), reflecting a high stress loading rate (~ 10 kPa/year) during the interseismic period (Pandey et al. 1995). Laboratory

experiments on quartzo-feldspathic rocks also show that the transition zone of coupling is characterized by temperature boundaries of 350 °C and 450 °C, implying that there is a thermally controlled downdip change from brittle–seismic to ductile–aseismic behavior (Hyndman 2013). The width of the transition zone is believed to be controlled by the geothermal gradient along the MHT, which in turn depends on the dip of the fault. A sharp transition zone usually indicates a relatively large dip angle for the MHT below the Higher Himalaya (Bilham et al. 2017).

5.3. Seismic Moment Accumulation and Release since the 1833 Earthquake

The moments released by known large earthquakes should equal the seismic moment deficit since the latest historical earthquake, assuming that only large earthquakes have contributed to strain release (Stevens and Avouac 2015). In central Nepal, the 1833 earthquake has been suggested to have been the latest large earthquake to occur prior to the 2015 Gorkha earthquake (Bilham 1995). It has been proposed that the epicenter of the 1833 earthquake was located northeast of Kathmandu, based on the orientations of the fractures and dikes that developed during the event (Mugnier et al. 2013). Bilham (1995) reported that the epicenter was probably north or northeast of Kathmandu, adjacent to the rupture zone of the 1934 earthquake. In contrast, Ambraseys and Douglas (2004) calculated an epicenter location for the 1833 earthquake nearly 40 km east of Kathmandu based on available macroseismic data. The uncertainty concerning the epicenter location for this event is in great part owing to the lack of records from eastern Nepal, precluding a reliable determination of the isoseismals (Mugnier et al. 2017). The magnitude of the 1833 earthquake is also poorly constrained, owing partly to the large uncertainty in the extent of the 1833 rupture. Bilham (1995) suggested that the extent of the 1833 earthquake reached to the northern part of the Kathmandu basin, with a maximal slip of 5–6 m, corresponding to a Mw 7.7 ± 0.2 event, which is somewhat greater than the value (M 7.3 ± 0.1) determined by Szeliga et al. (2010) using new intensity versus attenuation relations for

the Himalayan region. In addition, in the shallow part the rupture of the 1833 earthquake did not reach the surface, exhibiting similar characteristics to the 2015 Gorkha earthquake (Mugnier et al. 2011). These characteristics suggest that the 2015 earthquake may have occurred on the same segment of the décollement as the 1833 event. The 2015 Gorkha earthquake may have reruptured at least part, and perhaps all, of the portion of the décollement that slipped during the 1833 earthquake. Thus, the 1833 earthquake provides a critical window to understand the balance of the seismic moment accumulation and release.

Given the long-term slip rate and pattern of the interseismic coupling derived from this study, we estimate a seismic moment buildup rate $M_0 = 3.15 \pm 0.5 \times 10^{18}$ Nm/year (assuming a shear modulus of 30 GPa) in the central Nepalese Himalaya. This quantity is calculated from the area of the fault plane and the slip deficit rate on each patch. Based on the seismic moment buildup rate calculated above, we estimate an earthquake with an average slip of ~ 2.5 m is required to balance the strain accumulated since the 1833 earthquake. However, according to the coseismic slip distribution, the average slip during the 2015 Gorkha earthquake was greater than 4 m, and reached 7.8 m locally (Fig. 10a). This simple comparison suggests that the strain released in the 2015 Gorkha earthquake was considerably greater than the strain accumulated over the 182 years from 1833, which implies that the 1833 earthquake only partially released the strain that accumulated prior to that event. A fraction of the elastic energy that was not released during the 1833 event was finally released by the 2015 Gorkha earthquake. The partial strain released during an earthquake has been reported in western Nepal, where the 1505 M 8.5 earthquake occurred. The transient slip for the 1505 earthquake was over 9 m, while the accumulated displacement since the 1255 earthquake was approximately 5 m assuming a long-term shortening rate of ~ 20 mm/year, suggesting that nearly half of the strain accumulated before 1255 was not released by the Mw > 8 1255 earthquake (Mugnier et al. 2013).

The unbalance between the seismic moment accumulation and the release by large known earthquakes in central Nepal has important implications concerning the recurrence intervals of large Himalayan earthquakes. Assuming that the next earthquake in central Nepal has

the same spatial extent ($150 \text{ km} \times 60 \text{ km}$) and magnitude (Mw 7.9) as the Gorkha earthquake, a recurrence interval of ~ 200 years is estimated considering the average slip deficit rate of 14 mm/year from our coupling model. However, if the 2015 Gorkha earthquake also did not release all of the accumulated elastic strain, similar to the 1833 event, then the residual strain would reduce the recurrence interval of the next large earthquake near Kathmandu, and a realistic recurrence interval might be less than 200 years.

5.4. Implications for Earthquake Hazards in Central Nepal

The seismic risk in the central Nepalese Himalaya remains high, although the 2015 Gorkha earthquake partially released the accumulated strain. We calculated the coseismic static Coulomb stress change at a depth of 15 km triggered by the Gorkha earthquake using the expressions for calculating the stress field associated with angular dislocations provided by Meade (2007) (Fig. 11). This result clearly shows that the stress status adjacent to the rupture zone was perturbed by the Gorkha earthquake. To the south of the rupture zone, the coulomb stress calculations exhibited loading at a depth of 0–10 km, pushing this region ($\sim 150 \times 70 \text{ km}^2$) closer to failure. Geodetic measurements over the past 20 years suggest that this shallow décollement has been minimally affected by aseismic slip (e.g., slow slip events) and postseismic afterslip (Ader et al. 2012; Mencin et al. 2016; Sreejith et al. 2016; Gualandi et al. 2017). Thus, we believe that the strain accumulated in this portion will be released via large seismic events. Our coupling model suggests a slip deficit rate of 18 mm/year in this segment. The slip deficit in this shallow décollement could have exceeded 3.2 m since the 1833 event, which is sufficient to trigger an Mw ~ 8.0 earthquake. In addition, a 300 km long section to the west of the Gorkha earthquake has not undergone any earthquakes for 500 years, since the 1505 M ~ 8.5 earthquake. However, our model shows that this section is fully locked, with a downdip width of 110 km. The slip deficit could have exceeded 7.5 m based on a slip rate of 15 mm/year on the MHT, which is sufficient to fuel an Mw ~ 8.3 earthquake if a $150 \times 110 \text{ km}^2$ zone is ruptured.

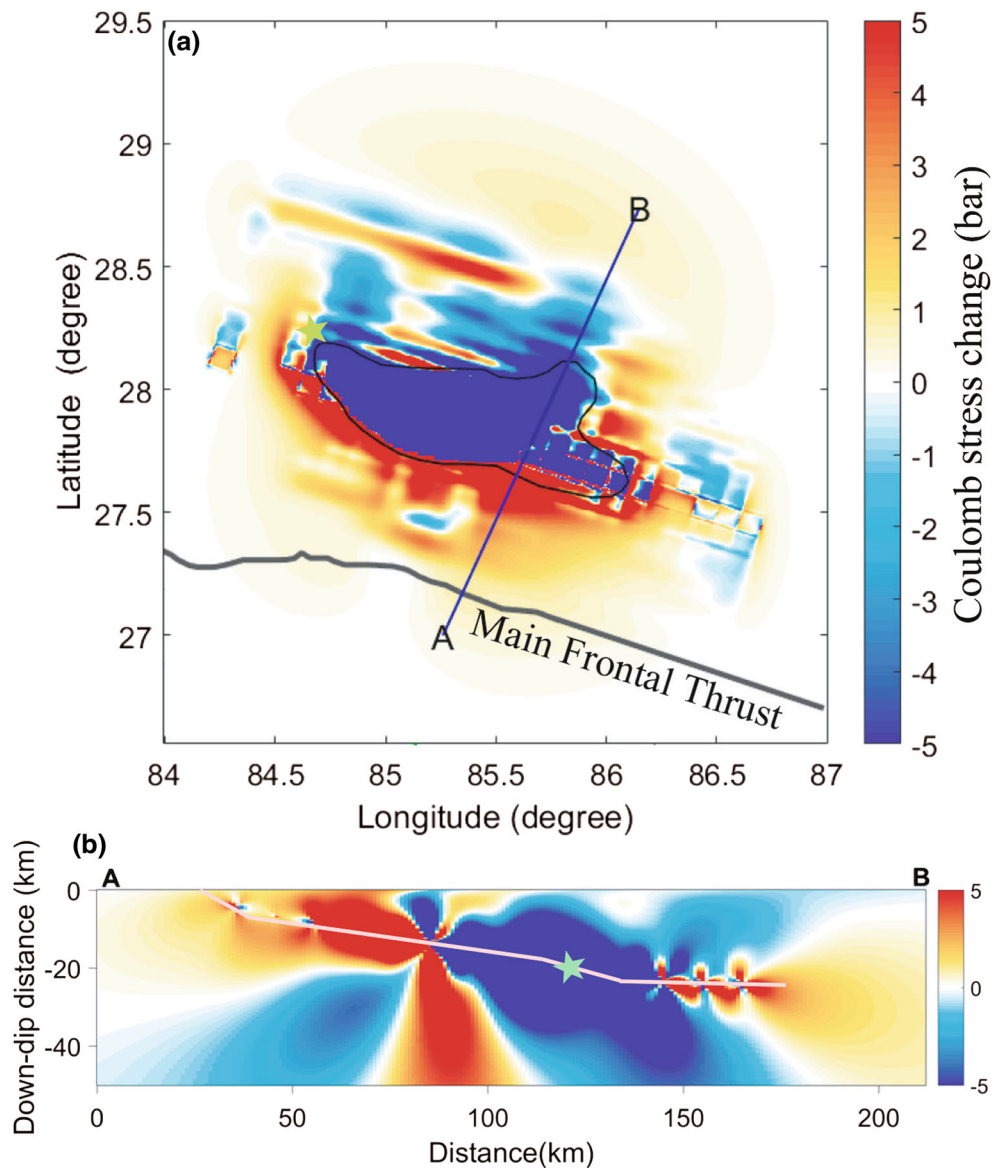


Figure 11

a Static Coulomb stress change at a depth of 15 km triggered by the Gorkha earthquake. Red areas denote stress loading and blue areas denote stress release. The black line outlines the coseismic slip of the mainshock. The yellow star shows the epicenter of the mainshock. **b** Cross-section with the Coulomb stress change calculated by the coseismic mainshock slip model. The white solid line denotes the interface of the MHT

6. Conclusions

The 2015 Gorkha Mw 7.9 earthquake highlights the urgent need to re-analyze the strain accumulation and release in Central Nepal. In this study, we incorporated GPS observations in southern Tibet with those publicly available for geodetic imaging of

interseismic coupling in the central Nepalese Himalaya. Our improved GPS measurements yield a convergence rate of 20.6 ± 1.6 mm/year in west-central Nepal, 17.4 ± 0.3 mm/year in central Nepal, and 16.9 ± 0.9 mm/year in eastern Nepal, exhibiting an along-strike variation of ~ 3 mm/year from west to east. The refined coupling model confirms the

finding of previous studies that the locking is essentially continuous throughout the MHT. In addition, we identified a sharp transition zone of the coupling ($0.2 < \phi < 1.0$) with an average width of ~ 50 km in the central Nepalese Himalaya. This transition zone coincides spatially with the location of the mid-crust ramp, suggesting that this ramp might control the deep transition from locked to creeping. We found that $\sim 85\%$ of the total moment released by the 2015 Gorkha earthquake was confined to the partially coupled transition portion of the MHT. This spatial correlation indicates that the earthquake mainly ruptured the brittle/ductile transition zone at the lower edge of the locked portion of the MHT.

Acknowledgements

We acknowledge the Crustal Movement Observation Network of China (CMONOC) for providing us with the GPS data in southern Tibet. We thank the editor Carla F. Braitenberg and two anonymous reviewers for their constructive and helpful comments, which greatly helped in improving our manuscript. This work is supported by the National Natural Science Foundation of China (41674015, 41731071, 41574012, 41674017, 41274037, 41541030), China postdoctoral science foundation (2016M592408), the Fundamental Research Funds for National Universities (CUG160225), Hubei Subsurface Multi-scale Imaging Key Laboratory (SMIL-2017-02) in China University of Geosciences, Wuhan, and Key Laboratory of Geospace Environment and Geodesy, Ministry of Education, Wuhan University (16-01-06). The figures are plotted using the Generic Mapping Tool (GMT) software.

Publisher's Note Springer Nature remains neutral with regard to jurisdictional claims in published maps and institutional affiliations.

REFERENCES

- Ader, T., Avouac, J.-P., Liu-Zeng, J., Lyon-Caen, H., Bollinger, L., Galetzka, J., et al. (2012). Convergence rate across the Nepal Himalaya and interseismic coupling on the Main Himalayan Thrust: Implications for seismic hazard. *Journal of Geophysical Research*, 117(B4), B04403. <https://doi.org/10.1029/2011jb009071>.
- Ambraseys, N. N., & Douglas, J. (2004). Magnitude calibration of north Indian earthquakes. *Geophysical Journal International*, 159, 165–206.
- Arora, B. R., Bansal, B. K., Prajapati, S. K., Sutar, A. K., & Nayak, S. (2017). Seismotectonics and seismogenesis of Mw7.8 Gorkha earthquake and its aftershocks. *Journal of Asian Earth Sciences*, 133, 2–11.
- Avouac, J. P. (2003). Mountain building, erosion, and the seismic cycle in the Nepal Himalaya. *Advances in Geophysics*, 46(03), 1–80.
- Avouac, J. P., Meng, L., Wei, S., Wang, T., & Ampuero, J.-P. (2015). Lower edge of locked Main Himalayan Thrust unzipped by the 2015 Gorkha earthquake. *Nature Geoscience*, 8(9), 708–711. <https://doi.org/10.1038/ngeo2518>.
- Bai, L., Liu, H., Ritsema, J., Mori, J., Zhang, T., Ishikawa, Y., et al. (2016). Faulting structure above the Main Himalayan Thrust as shown by relocated aftershocks of the 2015 Mw 7.8 Gorkha, Nepal, earthquake. *Geophysical Research Letters*, 43(2), 637–642.
- Banerjee, P., Bürgmann, R., Nagarajan, B., & Apel, E. (2008). Intraplate deformation of the Indian subcontinent. *Geophysical Research Letters*, 35(18), 7–12.
- Bettinelli, P., Avouac, J. P., Flouzat, M., Jouanne, F., Bollinger, L., Willis, P., et al. (2006). Plate motion of India and interseismic strain in the Nepal Himalaya from GPS and DORIS measurements. *Journal of Geodesy*, 80(8), 567–589. <https://doi.org/10.1007/s00190-006-0030-3>.
- Bilham, R. (1995). Location and magnitude of the 1833 Nepal earthquake and its relation to the rupture zones of contiguous great Himalayan earthquakes. *Current Science*, 69(2), 155–187.
- Bilham, R., & Ambraseys, N. (2005). Apparent Himalayan slip deficit from the summation of seismic moments for Himalayan earthquakes, 1500–2000. *Current Science*, 88(10), 1658–1663.
- Bilham, R., Larson, K., & Freymueller, J. (1997). GPS measurements of present-day convergence across the Nepal Himalaya. *Nature*, 386(6620), 61–64.
- Bilham, R., Mencin, D., Bendick, R., & Bürgmann, R. (2017). Implications for elastic energy storage in the Himalaya from the Gorkha 2015 earthquake and other incomplete ruptures of the Main Himalayan Thrust. *Quaternary International*, 462, 3–21.
- Bollinger, L., Avouac, J. P., Cattin, R., & Pandey, M. R. (2004). Stress buildup in the Himalaya. *Journal of Geophysical Research: Atmospheres*, 109(B11), 179–204.
- Cattin, R., & Avouac, J. P. (2000). Modeling mountain building and the seismic cycle in the Himalaya Nepal. *Journal of Geophysical Research: Solid Earth*, 105(B6), 13389–13407.
- Cheloni, D., D'Agostino, N., & Selvaggi, G. (2014). Interseismic coupling, seismic potential and earthquake recurrence on the southern front of the Eastern Alps (NE Italy). *Journal of Geophysical Research*, 119(5), 4448–4468.
- Chen, W. P., & Molnar, P. (1977). Seismic moments of major earthquakes and the average rate of slip in central Asia. *Journal of Geophysical Research: Atmospheres*, 82(20), 2945–2970.
- Chlieh, M., Perfettini, H., Tavera, H., Avouac, J. P., Remy, D., Nocquet, J. M., et al. (2011). Interseismic coupling and seismic potential along the Central Andes subduction zone. *Journal of Geophysical Research: Solid Earth*, 116(B12), 12405.

- Duputel, Z., Vergne, J., Rivera, L., Wittlinger, G., Farra, V., & Hetényi, G. (2016). The 2015 Gorkha earthquake: A large event illuminating the Main Himalayan Thrust fault. *Geophysical Research Letters*, *43*(6), 2517–2525. <https://doi.org/10.1002/2016gl068083>.
- Elliott, J. R., Jolivet, R., González, P. J., Avouac, J. P., Hollingsworth, J., Searle, M. P., et al. (2016). Himalayan megathrust geometry and relation to topography revealed by the Gorkha earthquake. *Nature Geoscience*, *9*(2), 174–180. <https://doi.org/10.1038/ngeo2623>.
- Feldl, N., & Bilham, R. (2006). Great Himalayan earthquakes and the Tibetan plateau. *Nature*, *444*(7116), 165–170.
- Freund, L. B., & Barnett, D. M. (1976). A two-dimensional analysis of surface deformation due to dip-slip faulting. *Bulletin of the Seismological Society of America*, *66*(3), 667–675.
- Fu, Y., & Freymueller, J. T. (2012). Seasonal and long-term vertical deformation in the Nepal Himalaya constrained by GPS and GRACE measurements. *Journal of Geophysical Research: Solid Earth*, *117*, B03407. <https://doi.org/10.1029/2011JB008925>.
- Galetzka, J., Melgar, D., Genrich, J. F., Geng, J., Owen, S., Lindsey, E. O., et al. (2015). Slip pulse and resonance of the Kathmandu basin during the 2015 Gorkha earthquake. *Nepal. Science*, *349*(6252), 1091–1095. <https://doi.org/10.1126/science.aac6383>.
- Grandin, R., Doin, M.-P., Bollinger, L., Pinel-Puysségur, B., Ducret, G., Jolivet, R., et al. (2012). Long-term growth of the Himalaya inferred from interseismic InSAR measurement. *Geology*, *40*(12), 1059–1062. <https://doi.org/10.1130/g33154.1>.
- Grandin, R., Vallée, M., Satriano, C., Lacassin, R., Klinger, Y., Simoes, M., et al. (2015). Rupture process of the Mw = 7.9 2015 Gorkha earthquake (Nepal): Insights into Himalayan megathrust segmentation. *Geophysical Research Letters*, *42*(20), 8373–8382.
- Gualandi, A., Avouac, J.-P., Galetzka, J., Genrich, J. F., Blewitt, G., Adhikari, L. B., et al. (2017). Pre- and post-seismic deformation related to the 2015, Mw 7.8 Gorkha earthquake. *Nepal. Tectonophysics*, *714–715*, 90–106.
- He, P., Wang, Q., Ding, K., Wang, M., Qiao, X., Li, J., et al. (2016). Source model of the 2015 Mw 6.4 Pishan earthquake constrained by interferometric synthetic aperture radar and GPS: Insight into blind rupture in the western Kunlun Shan. *Geophysical Research Letters*, *43*(4), 1511–1519.
- Hyndman, R. D. (2013). Downdip landward limit of Cascadia great earthquake rupture. *Journal of Geophysical Research: Solid Earth*, *118*(10), 5530–5549.
- Jackson, M., & Bilham, R. (1994). Constraints on Himalayan deformation inferred from vertical velocity fields in Nepal and Tibet. *Journal of Geophysical Research: Solid Earth*, *99*(B7), 13897–13912. <https://doi.org/10.1029/94JB00714>.
- Jouanne, F., Mugnier, J. L., Gamond, J. F., Fort, P. L., Pandey, M. R., Bollinger, L., et al. (2004). Current shortening across the Himalayas of Nepal. *Geophysical Journal International*, *157*(1), 1–14. <https://doi.org/10.1111/j.1365-246X.2004.02180.x>.
- Jouanne, F., Mugnier, J. L., Sapkota, S. N., Bascou, P., & Pecher, A. (2017). Estimation of coupling along the Main Himalayan Thrust in the central Himalaya. *Journal of Asian Earth Sciences*, *133*, 62–71.
- Kumar, S., Wesnousky, S. G., Jayangondaperumal, R., Nakata, T., Kumahara, Y., & Singh, V. (2010). Paleoseismological evidence of surface faulting along the northeastern Himalayan front, India: Timing, size, and spatial extent of great earthquakes. *Journal of Geophysical Research: Solid Earth*, *115*, B12422. <https://doi.org/10.1029/2009JB006789>.
- Lavé, J., & Avouac, J. P. (2000). Active folding of fluvial terraces across the Siwaliks Hills, Himalayas of central Nepal. *Journal of Geophysical Research: Solid Earth*, *105*(B3), 5735–5770.
- Lavé, J., & Avouac, J. P. (2001). Fluvial incision and tectonic uplift across the Himalayas of central Nepal. *Journal of Geophysical Research: Solid Earth*, *106*(B11), 26561–26591.
- Lawson, C. L., & Hanson, R. J. (1974). *Solving least squares problems*. Prentice-Hall, 77(1), 673–682.
- Lay, T., Kanamori, H., Ammon, C. J., Koper, K. D., Hutko, A. R., Ye, L., et al. (2012). Depth-varying rupture properties of subduction zone megathrust faults. *Journal of Geophysical Research: Solid Earth*, *117*, B04311. <https://doi.org/10.1029/2011JB009133>.
- Liang, S., Gan, W., Shen, C., Xiao, G., Liu, J., Chen, W., et al. (2013). Three-dimensional velocity field of present-day crustal motion of the Tibetan Plateau derived from GPS measurements. *Journal of Geophysical Research: Solid Earth*, *118*(10), 5722–5732.
- Lorenzo-Martín, F., Roth, F., & Wang, R. (2006). Inversion for rheological parameters from post-seismic surface deformation associated with the 1960 Valdivia earthquake, Chile. *Geophysical Journal International*, *164*(1), 75–87.
- Maerten, F. (2005). Inverting for slip on three-dimensional fault surfaces using angular dislocations. *Bulletin of the Seismological Society of America*, *95*(5), 1654–1665.
- McNamara, D. E., Yeck, W. L., Barnhart, W. D., Schulte-Pelkum, V., Bergman, E., Adhikari, L. B., et al. (2017). Source modeling of the 2015 Mw 7.8 Nepal (Gorkha) earthquake sequence: Implications for geodynamics and earthquake hazards. *Tectonophysics*, *714–715*, 21–30. <https://doi.org/10.1016/j.tecto.2016.08.004>.
- Meade, B. J. (2007). Algorithms for the calculation of exact displacements, strains, and stresses for triangular dislocation elements in a uniform elastic half space. *Computers & Geosciences*, *33*(8), 1064–1075.
- Mencin, D., Bendick, R., Upreti, B. N., Adhikari, D. P., Gajurel, Ananta P., Bhattarai, R. R., et al. (2016). Himalayan strain reservoir inferred from limited afterslip following the Gorkha earthquake. *Nature Geoscience*, *9*, 533–537. <https://doi.org/10.1038/ngeo2734>.
- Métis, M., Socquet, A., & Vigny, C. (2012). Interseismic coupling, segmentation and mechanical behavior of the central Chile subduction zone. *Journal of Geophysical Research: Solid Earth*, *117*(B3), B03406. <https://doi.org/10.1029/2011JB008736>.
- Molnar, P., & Chen, W. P. (1984). S–P wave travel time residuals and lateral inhomogeneity in the mantle beneath Tibet and the Himalaya. *Journal of Geophysical Research: Atmospheres*, *89*(B8), 6911–6917.
- Molnar, P., & Tapponnier, P. (1975). Cenozoic tectonics of Asia: Effects of a continental collision: Features of recent continental tectonics in Asia can be interpreted as results of the India–Eurasia collision. *Science*, *189*(4201), 419–426.
- Morsut, F., Pivetta, T., Braitenberg, C., & Poretti, G. (2017). Strain Accumulation and Release of the Gorkha, Nepal, Earthquake (Mw 7.8, 25 April 2015). *Pure and Applied Geophysics*, *175*(5), 1909–1923.
- Mugnier, J. L., Gajurel, A., Huyghe, P., Jayangondaperumal, R., Jouanne, F., & Upreti, B. (2013). Structural interpretation of the

- great earthquakes of the last millennium in the central Himalaya. *Earth-Science Reviews*, 127(1), 30–47.
- Mugnier, J. L., Huyghe, P., Gajurel, A. P., Upreti, B. N., & Jouanne, F. (2011). Seismites in the Kathmandu basin and seismic hazard in central Himalaya. *Tectonophysics*, 509(1), 33–49.
- Mugnier, J. L., Jouanne, F., Bhattarai, R., Cortes-Aranda, J., Gajurel, A., Leturmy, P., et al. (2017). Segmentation of the Himalayan megathrust around the Gorkha earthquake (25 April 2015) in Nepal. *Journal of Asian Earth Science*, 141, 236–252. <https://doi.org/10.1016/j.jseae.2017.01.015>.
- Nábělek, J., Hetényi, G., Vergne, J., Sapkota, S., Kafle, B., Jiang, M., et al. (2009). Underplating in the Himalaya-Tibet collision zone revealed by the Hi-CLIMB experiment. *Science*, 325(5946), 1371–1374.
- Pandey, M. R., Tandukar, R. P., Avouac, J. P., Lave, J., & Massot, J. P. (1995). Interseismic strain accumulation on the Himalaya crustal ramp (Nepal). *Geophysical Research Letters*, 22, 751–754. <https://doi.org/10.1029/94GL02971>.
- Pollitz, F. F. (2014). Post-earthquake relaxation using a spectral element method: 2.5-D case. *Geophysical Journal International*, 198(1), 308–326.
- Prawirodirdjo, L., McCaffrey, R., Chadwell, C. D., Bock, Y., & Subarya, C. (2010). Geodetic observations of an earthquake cycle at the Sumatra subduction zone: Role of interseismic strain segmentation. *Journal of Geophysical Research: Solid Earth*, 115(B3), 153–164.
- Sapkota, S. N., Bollinger, L., Klinger, Y., Tapponnier, P., Gaudemier, Y., & Tiwari, D. (2013). Primary surface ruptures of the great Himalayan earthquakes in 1934 and 1255. *Nature Geoscience*, 6(1), 71–76. <https://doi.org/10.1038/ngeo1669>.
- Savage, J. C. (1983). A dislocation model of strain accumulation and release at a subduction zone. *Journal of Geophysical Research: Solid Earth*, 88(B6), 4984–4996.
- Sreejith, K. M., Sunil, P. S., Agrawal, R., Saji, A. P., Ramesh, D. S., & Rajawat, A. S. (2016). Coseismic and early postseismic deformation due to the 25 April 2015, Mw 7.8 Gorkha, Nepal, earthquake from InSAR and GPS measurements. *Geophysical Research Letters*, 43(7), 3160–3168.
- Stevens, V. L., & Avouac, J. P. (2015). Interseismic coupling on the main Himalayan thrust. *Geophysical Research Letters*, 42(14), 5828–5837. <https://doi.org/10.1002/2015gl064845>.
- Stevens, V. L., & Avouac, J. P. (2016). Millenary Mw > 9.0 earthquakes required by geodetic strain in the Himalaya. *Geophysical Research Letters*, 43(3), 1118–1123.
- Suwa, Y., Miura, S., Hasegawa, A., Sato, T., & Tachibana, K. (2006). Interplate coupling beneath NE Japan inferred from three-dimensional displacement field. *Journal of Geophysical Research: Atmospheres*, 111(B4), 258–273.
- Szeliga, W., Hough, S., Martin, S., & Bilham, R. (2010). Intensity, magnitude, location, and attenuation in India for felt earthquakes since 1762. *Bulletin of the Seismological Society of America*, 100(2), 570–584.
- Tan, K., Zhao, B., Zhang, C. H., Du, R. L., Wang, Q., Huang, Y., et al. (2016). Rupture models of the Nepal Mw 7.9 earthquake and Mw 7.3 aftershock constrained by GPS and InSAR coseismic deformations. *Chinese Journal of Geophysics*, 59(6), 2080–2093. (in Chinese).
- Vergne, J., Cattin, R., & Avouac, J. P. (2001). On the use of dislocations to model interseismic strain and stress build-up at intracontinental thrust faults. *Geophysical Journal International*, 147(1), 155–162. <https://doi.org/10.1046/j.1365-246X.2001.00524.x>.
- Vergnolle, M., Pollitz, F., & Calais, E. (2003). Constraints on the viscosity of the continental crust and mantle from GPS measurements and postseismic deformation models in western Mongolia. *Journal of Geophysical Research: Solid Earth*, 108(B10), 2502. <https://doi.org/10.1029/2002JB002374>.
- Wang, K., & Fialko, Y. (2018). Observations and modeling of coseismic and postseismic deformation due to the 2015 Mw 7.8 Gorkha (Nepal) earthquake. *Journal of Geophysical Research: Solid Earth*, 123(1), 761–779.
- Wang, W., Qiao, X., Yang, S., & Wang, D. (2017). Present-day velocity field and block kinematics of Tibetan Plateau from GPS measurements. *Geophysical Journal International*, 208, 1088–1102.
- Wang, Q., Zhang, P. Z., Freymueller, J. T., Bilham, R., Larson, K. M., Lai, X., et al. (2001). Present-day crustal deformation in China constrained by global positioning system measurements. *Science*, 294(5542), 574–577.
- Xiong, W., Tan, K., Qiao, X., Liu, G., Nie, Z., & Yang, S. (2017). Coseismic, postseismic and interseismic coulomb stress evolution along the Himalayan main frontal thrust since 1803. *Pure and Applied Geophysics*, 174(5), 1889–1905.
- Xu, C., Ding, K., Cai, J., & Grafarend, E. W. (2009). Methods of determining weight scaling factors for geodetic–geophysical joint inversion. *Journal of Geodynamics*, 47(1), 39–46.
- Yi, L., Xu, C., Zhang, X., Wen, Y., Jiang, G., Li, M., et al. (2017). Joint inversion of GPS, InSAR and teleseismic data sets for the rupture process of the 2015 Gorkha, Nepal, earthquake using a generalized ABIC method. *Journal of Asian Earth Sciences*, 148, 121–130.
- Zhao, B., Bürgmann, R., Wang, D., Tan, K., Du, R., & Zhang, R. (2017). Dominant controls of downdip afterslip and viscous relaxation on the postseismic displacements following the Mw 7.9 Gorkha, Nepal, earthquake. *Journal of Geophysical Research: Solid Earth*, 122(10), 8376–8401.
- Zhao, W., Nelson, K. D., Che, J., Quo, J., Lu, D., Wu, C., et al. (1993). Deep seismic reflection evidence for continental underthrusting beneath southern Tibet. *Nature*, 366(6455), 557–559.
- Zumberge, J. F., Hefflin, M. B., Jefferson, D. C., Watkins, M. M., & Webb, F. H. (1997). Precise point positioning for the efficient and robust analysis of GPS data from large networks. *Journal of Geophysical Research: Solid Earth*, 102(B3), 5005–5017.